Modeling, Control and Implementation of Adaptive Reconfigurable ROtary Wings (ARROWs)

Xinyu Cai, Shane Kyi Hla Win, Hitesh Bhardwaj, and Shaohui Foong, *Member, IEEE*

***Abstract*—Inspired by the self-rotating motion of the descending maple seeds, we introduce a novel modular aerial robotic platform—ARROWs. With customized wing and control modules, ARROWs can be easily reassembled into different configurations. Unlike conventional multirotor aerial vehicles which rely on the direct thrust from propellers, ARROWs can generate more lift by their revolving wings. However, the complex dynamics causes difficulties in flight controller development. In this work, we first analyze the flight dynamics by considering a combination of effects from the propeller, aerodynamic force on the wing, as well as self-rotating motion. As a result, a cascaded flight controller with a unified framework is designed based on reduced flight dynamics and relaxed hovering conditions to achieve stable flights in all proposed configurations. In addition, a set of inertial measurement units is employed for each flight module to estimate the flight configuration to overcome the dynamic uncertainties caused by manual reconstruction. Finally, our proposed platform and flight control strategy are validated using several flight experiments in 12 different configurations (include both centrosymmetric and centrally asymmetric cases). The results show an average position error of 8.9 cm with a deviation of 2.4 cm among all configurations in hovering tests.**

***Index Terms*—Modular aerial robotics, motion control, unmanned aerial vehicle.**

I. Introduction

With applications in a growing number of industries, aerial vehicles have gathered increased interest from scientists and engineers [1], [2]. Thanks to recent achievements in robotic platforms and control technology, aerial vehicles are expected to perform with more functionalities to accomplish more complex tasks. As a result, aerial robots capable of reconfiguration [3], [4], [5], [6], [7], multiple modes of locomotion [8], robotic swarm [9], self-navigation [10], resilience [11], transformation [12], [13], [14], [15], [16], [17], and cooperative working [18] have been widely studied with great achievements in recent years. The significant potential of multiple functionalities in robotic platforms can be also seen in ground and water robots [19], [20], [21], [22], [23]. For example, in [20], a large modular floating structure system (known as tactically expandable maritime platform) was self-assembled by a team of robotic boats in the open ocean for maritime applications. Unlike ground and water robots, dynamic uncertainties caused by reconfigurations pose a challenge for achieving modularity in aerial robot platforms, leading to more difficulties in attitude stabilization in flight. Still, some interesting studies have been made [3], [4], [5], [6], [24]. Based on a quadrotor platform, a modular flying structure (known as ModQuad) was developed with the ability for self-assembly [4] and self-disassembly [24] in midair. Other reported modular aerial robotic platforms such as universal flying objects [3], distributed flight array [5], and the "SplitFlyer" [6] can achieve stable flights, but require at least two actuators to stabilize the flight attitude.

To seek a simpler flight unit, efforts have been made to explore the control and attitude stabilization strategy for underactuated flight systems. Study in [25] showed how a normal quadcopter maintained a safe flight after one or two rotors had failed. More severe underactuated aerial systems with only one actuator have been developed and validated to be able to track 3-D position, such as "monospinner" in [26], single actuator microaerial vehicle in [27], and swashplateless microair vehicle in [28]. Instead of actively stabilizing the flight attitude, the nature inspired robotic samara [29], [30], [31] shows a different strategy by making use of its winged body to obtain both extra lift force and passive attitude stability in flight [32], [33], [34].

Even though the current publications on rotating winged aerial robots indicated some promising abilities such as position tracking, modularity, as well as high hovering efficiency, it still remains challenging for practical implementation. One critical reason is that their position tracking ability is highly rely on the passive stability due to the severe underactuation. In other words, extra payloads might change their mass or inertial distribution, resulting in weak or absent of flight stabilization ability. In addition, the single functionality also limits their potential

Manuscript received 2 June 2022; revised 21 October 2022 and 7 December 2022; accepted 15 December 2022. Date of publication 26 January 2023; date of current version 16 August 2023. Recommended by Technical Editor H. Son and Senior Editor W. J. C. Zhang. *(Corresponding author: Shaohui Foong.)*

The authors are with the Engineering Product Development Pillar, Singapore University of Technology and Design, Singapore 487372 (e-mail: xinyu_cai@mymail.sutd.edu.sg; hlawin_kyi@sutd.edu.sg; hitesh_bhardwaj@mymail.sutd.edu.sg; foongshaohui@sutd.edu.sg).

This article has supplementary material provided by the authors and color versions of one or more figures available at https://doi.org/10.1109/TMECH.2023.3235346.

Digital Object Identifier 10.1109/TMECH.2023.3235346

applications to some simple scenarios. For example, those robots can only work with their designed parameters such as footprint, payload capacity, and rotating speed in hovering.

With the purpose of expanding the application of the single actuator monocopter, our previous study [34] introduced modular single actuator monocopter that featured a cooperative mode and a controlled passive separation. However, both the singular and cooperative configurations rely on the inherited passive attitude stability [32] in the flight. With the passive stability, the robot is able to recover from disturbance to its equilibrium state without active controlling. In this way, the positioning control can be easily achieved by generating a cyclic controlling signal to the propeller to drive the robot to move in the desired direction.

In this work, we introduce Adaptive Reconfigurable ROtary Wings (ARROWs) with emphasis on modularity and reconfigurability [an example of prototype can be found in Fig. 1(c)]. With simple manual assistance, ARROWs can be reassembled into various configurations by different combinations of basis repeatable modules [in Fig. 1(a)]. This enables the ARROWs to be adaptive to different types of the working environments and user's requirements. For example, a suitable footprint, payload capacity, flight duration, and rotating speed can be selected by different combinations of wing numbers and the pitching angles. To this end, a close-looped attitude controller needs to be developed to actively stabilize the flight posture. Motivated by [25] and [35], we developed attitude controller to stabilize the primary axis in the flight. Based on the reduced flight dynamics and relaxed hovering conditions, a cascaded structure is proposed for position control. For the implementation of the proposed flight controller, the uncertainty of parameters caused by reconfiguration is tackled by employing a set of inertial measurement units (IMUs) and manual trim flights.

Compared to the conventional multirotor aerial vehicles, which has ability to fully control its flight attitude, the winged rotating robot need to sacrifice its yaw motion to obtain more hovering efficiency or overcome the underactuation. As a result, the potential application of ARROWs may be limited. Yet, some recent studies show great promise by taking advantage of the passive revolving motion, such as the Flydar–Flying Light Detection and Ranging (Li-DAR) [36]. Besides, [31] also highlighted a wider view of a normal camera by using the rotating wing robot, which indicates the potential of higher working efficiency in unknown environment exploring and mapping. More applications can be expected with reliable and robust self-rotating winged aerial robotic platforms.

The rest of this article is organized as follows. In Section II, we detail the modular design, prototype fabrication, and flight characteristics of ARROWs. In Section III, an aerodynamic model for propellers and wings is studied. Based on the relaxed hovering condition, flight equilibrium, and reduced flight dynamics are introduced. With these insights, we develop a cascaded flight controller with an attitude controller and translational controller in Section IV. Considering the difficulties caused by the modular design, strategies such as parameter estimation and trim flights are introduced to implement the proposed flight controller as well. To verify the feasibility of the reported modular robotic platform and controlling law, a total of 12 different configurations constructed by repeatable units are tested with hovering, step, and helix trajectory flights in Section V. Finally, Section VI concludes the article.

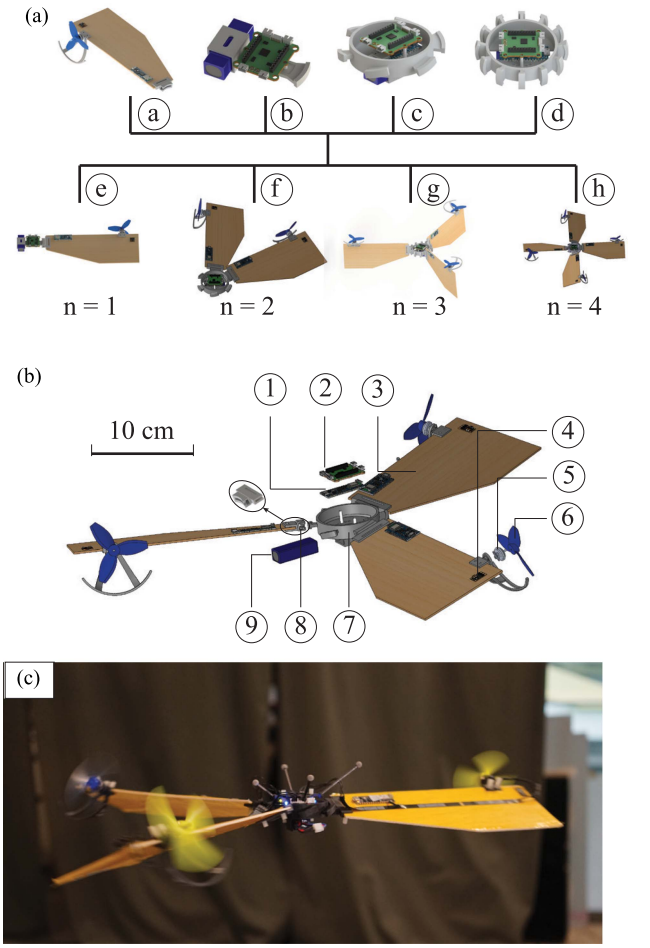

Fig. 1. (a) illustrates the concept of modular design. ⓐ shows the wing module. ⓑ, ⓒ, and ⓓ show different type of control modules. ⓔ, ⓕ, ⓖ, and ⓗ show examples of different combinations of control module and wing module when the number of wing module $n = 1, 2, 3$, and 4 respectively. (b) shows details of the components of control module and wing module. ① inertial measurement unit, ② flight controller, ⑦ frame of control module, and ⑨ battery form the control module. ③ wing profile, ④ electronic speed controller, ⑤ brushless motor, ⑥ propeller, and ⑧ connector compose the wing module. (c) shows a photo of prototype [$n = 3$, centrally asymmetric configuration, details shown in Fig. 6(g)] in flight. The tangential forces of propellers mounted on the wing provide sufficient torque to drive the rotating motion. The rotating wings generate most of the thrust for hovering. The torques generated by the normal forces of propellers also stabilize the flight attitude.

II. Platform Description

A. Modular Design

ARROWs consists of one control module and multiple wing modules $n \geq 1$ (while the maximum n is limited by practicality). The control module primarily includes a flight controller and a battery. In addition, we employ an extra IMU (different to the one used for attitude stabilization) for preflight parameter estimation for an unknown configuration. We created three types

of control modules suitable for showing examples of different configuration (shown in Fig. 1. (a) ⓑ, ⓒ, and ⓓ). The wing modules [Fig. 1. (a) ⓐ] are considered to be identical and consists of a brushless motor, a wing, a propeller, an electronic speed controller to drive the brushless motor as well as an extra IMU with the same purpose as one in the control module.

In order to achieve the modularity and reconfigurability, we design a T-shape male and female connectors with curved surface [shown in Fig. 1(b)⑧]. The control module and wing modules can be manually disassembled and reconnected into different configurations with sufficient rigidity for flight. The combination of both the control module and wing modules form the flight airframe of ARROWs.

B. Prototype Fabrication

The details of components of prototype fabrication can be referred to in Fig. 1(b). The customized frame of the control module and wing module are modeled by CAD software (SOLIDWORKS) and printed by a 3-D printer (Markforged) with Onyx (a composite 3-D printing material) (⑦ and ⑧). And the wing (③) is fabricated from a piece of balsa wood (230 mm × 100 mm × 2 mm) covered with Kapton tape. An assembled prototype is shown in Fig. 1(c) with three repeatable wing modules in flight.

C. System Characteristic

As discussed in previous sections, we have shown that the flight mode of ARROWs is different from conventional multirotor aerial robots. The tangential component of propeller thrust causes the rotating motion, which allows the wing module to produce higher thrust than using the propeller directly.

Furthermore, ARROWs is able to fly in 3-D space in a severely underactuated condition with only one actuator. This is owing to the passive stability of its attitude dynamics, which is a result of the aerodynamic force produced by the wing in rotating motion.

Without loss of generality, we also consider the configuration when pitching angle $\theta = 90$ (degrees) and number of wing modules $n \geq 3$, which generates the lifting force directly from the propeller. Since all propellers spin in the same direction (clockwise), an unbalanced torque results in its z axis. We find that the normalized average motor command used in configuration (f) and (i) (refer to Fig. 6) are 48.2% and 58%, respectively, indicating that ARROWs becomes more power efficient by making use of the wing. The flight efficiency is also validated by the flight duration test in Table II.

III. Flight Dynamics

A. Force and Torque Generation

In this study, we show a modular aerial robotic platform, which consists of a control module and n ($n \geq 1$) wing modules. The rotating motion of the robot allows both propeller and wing to generate force and torque. In this section, we aim to show how the force and torque are produced by the propeller and wing, respectively, in the wing module's frame. As shown in Fig. 2(a), a motor with a propeller is rigidly attached to the leading edge

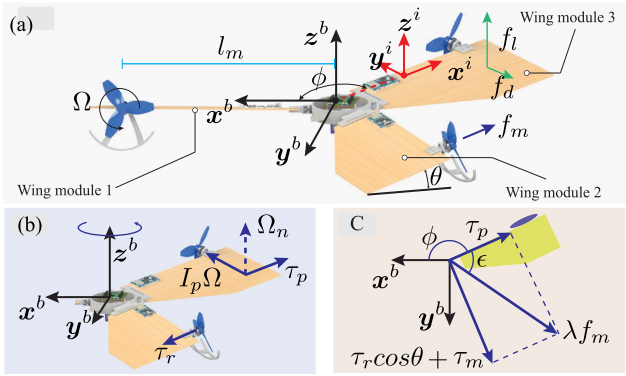

Fig. 2. Forces and torques generated by ARROWs. (a) shows the details of how the forces are generated by the propeller and the rotating wing. (b) shows how the torques are generated due to precession motion and propeller. (c) is the top view of (a), illustrating how the torque generated on wing module 3 by a propeller is approximated by defining parameters ϵ and λ.

of the wing and the force generated by the propeller is parallel to the y axis of the wing's frame. Let f_m and τ_r denote the force and reaction torque generated by the propeller, formulated by

$$f_m = c_F \Omega^2, \quad \tau_r = c_T \Omega^2 \tag{1}$$

where c_F and c_T are propeller's force and torque coefficients, respectively, Ω is the scalar angular rate of the propeller. Unlike other aerial robots, ARROWs also experience a significant aerodynamic force due to the revolving wing profile. By employing Blade element theory [37], the lift (f_l) and drag (f_d) forces generated by a wing element $\mathrm{d}r$ at the radial position r can be modeled by

$$\mathrm{d}f_l = \frac{1}{2}\rho C_l c(r) V^2(r) \mathrm{d}r, \quad \mathrm{d}f_d = \frac{1}{2}\rho C_d c(r) V^2(r) \mathrm{d}r \tag{2}$$

where ρ is the air density; c(r) is the chord function of wing geometry; C_l and C_d are lift and drag coefficients, respectively. V is translational velocity related to the inertia frame. To simplify the consideration, we use lift f_l and drag f_d force acting on center of pressure of the wing to approximate the sum of aerodynamic forces. As f_l and f_d are dependent on lift C_l, drag C_d coefficients, and the relative air speed V. In the vertical configuration when $\theta = 90°$, both the relative air speed (V) and lift coefficient C_l in (2) become small [38]. Therefore, in this case, we assume the lift force $f_l \approx 0$. Thereafter, the aerodynamic forces can be decomposed into normal (f_n) and tangential (f_t) components, as

$$f_n = f_l \cos\theta + f_d \sin\theta, \quad f_t = f_l \sin\theta + f_d \cos\theta \tag{3}$$

where θ is the pitch angle of the wing [Fig. 2(a)].

The spinning motor-propeller also rotates with the body frame around its primary axis at a non-zero speed, generating an extra torque $\boldsymbol{\tau}_p$ due to the precession motion [39]. To model this torque, let $\boldsymbol{I}_p$ denote the moment of inertia of the motor-propeller, $\boldsymbol{\Omega}$ denote the spin vector, $\boldsymbol{\Omega}_p$ denote the precession vector, then the precession torque can be formulated by

$$\boldsymbol{\tau}_p = \boldsymbol{\Omega}_p \times \boldsymbol{I}_p \boldsymbol{\Omega} \tag{4}$$

which shows that the magnitude of precession torque is related to spinning speed of motor-propeller, rotating speed of robot's body frame and the angle between spin vector $\boldsymbol{\Omega}$ and precession vector $\boldsymbol{\Omega}_p$. Its direction is perpendicular to both the spin vector and precession vector and follows right-hand rule.

B. Translational Dynamics

With the force and torque described in Section III-A, we derive the full translational dynamics. Let $\boldsymbol{R}_i^b$, a 3×3 rotation matrix, represent the rotation from ith wing module to control module. Similarly, let $\boldsymbol{R}_b^w = [\boldsymbol{i}, \boldsymbol{j}, \boldsymbol{k}]$, a 3×3 rotation matrix, map the rotation from body frame to world frame, where $\boldsymbol{i}, \boldsymbol{j}, \boldsymbol{k}$ are the corresponding vectors of three body axes in the inertia frame.

We use vectors $\boldsymbol{f}_{m,i} = [0, f_{m,i}, 0]^T$ and $\boldsymbol{f}_{a,i} = [0, -f_{t,i}, f_{n,i}]^T$ to denote the forces generated by propeller and wing respectively in ith wing module's frame. Let $\boldsymbol{r} = [r_x, r_y, r_z]^T$ denote the position of the robot in the world frame and m denote the total mass of the robot. Then, the translational dynamics can be simply written by applying Newton's law, as

$$m\ddot{\boldsymbol{r}} = \boldsymbol{R}_b^w \sum \boldsymbol{R}_i^b (\boldsymbol{f}_{m,i} + \boldsymbol{f}_{a,i}) - mg\boldsymbol{e}_3 \tag{5}$$

where g represents gravitational constant, and $\boldsymbol{e}_3 = [0, 0, 1]^T$ is a basis vector.

C. Attitude Dynamics

To formulate the torque produced by ith propeller's thrust $\boldsymbol{f}_{m,i}$ and wing's aerodynamic force $\boldsymbol{f}_{a,i}$, we use $\boldsymbol{l}_{m,i}$ and $\boldsymbol{l}_{a,i}$ to denote the location of propeller and center of pressure with respect to control module's frame. The torques can be calculated by $\boldsymbol{\tau}_{m,i} = \boldsymbol{l}_{m,i} \times (\boldsymbol{R}_i^b \boldsymbol{f}_{m,i})$ and $\boldsymbol{\tau}_{a,i} = \boldsymbol{l}_{a,i} \times (\boldsymbol{R}_i^b \boldsymbol{f}_{a,i})$, respectively.

Let $\boldsymbol{\Omega}_n$ denote the rotation axis in robot's body frame, then the torque caused by precession motion can be obtained by modifying (4), as $\boldsymbol{\tau}_{p,i} = \boldsymbol{\Omega}_n \times \boldsymbol{R}_i^b \boldsymbol{I}_{p,i} \boldsymbol{\Omega}_i$, where the moment of inertia of all motor-propeller $\boldsymbol{I}_{p,i}$ are considered as identical. The reaction torque produced by ith propeller in body frame can be simply given as $\boldsymbol{\tau}_{r,i} = \boldsymbol{R}_i^b [0, -\tau_{r,i}, 0]^T$, where τ_r is introduced in (1).

Like other rigid bodies, the attitude dynamics of ARROWs can also be written by Euler's equation

$$\sum_i (\boldsymbol{\tau}_{m,i} + \boldsymbol{\tau}_{a,i} + \boldsymbol{\tau}_{p,i} + \boldsymbol{\tau}_{r,i}) = \boldsymbol{I}\dot{\boldsymbol{\omega}} + \boldsymbol{\omega}_\times \boldsymbol{I}\boldsymbol{\omega} \tag{6}$$

where $\boldsymbol{I} = \mathrm{diag}(I_x, I_y, I_z)$ is the total moment of inertia of the robot and $\boldsymbol{\omega} = [\omega_x, \omega_y, \omega_z]^T$ is the angular velocity with respect to the body frame.

D. Relaxed Hover Solution

Instead of using a set of specific angles (such as Euler angles), we define a body fixed rotation axis to represent its attitude in the flight, $\boldsymbol{\Omega}_n = \Omega_n \boldsymbol{n}$, where $\boldsymbol{n}$ is a unit vector, Ω_n represents the scalar rotation speed. When the robot rotates at a relatively high speed Ω_n, the force components which are perpendicular to $\boldsymbol{n}$ are considered to be zero on average over a rotation cycle, which allows us to use the force components parallel to $\boldsymbol{n}$ to represent the collective force in body frame. As a result, the relaxed hovering condition necessitates

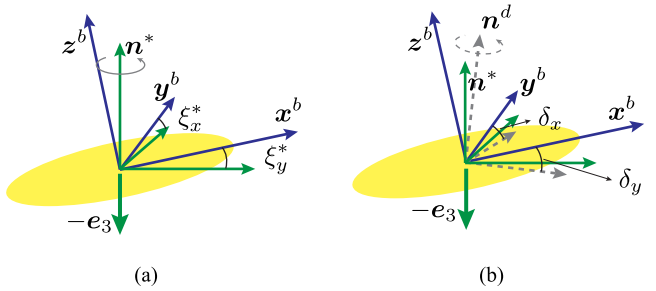

Fig. 3. (a) shows the relaxed hover condition of ARROWs with rotating axis $\boldsymbol{n}^*$. ξ_x^* and ξ_y^* denote the angular deviation of $\boldsymbol{n}^*$ and $\boldsymbol{z}^b$. (b) shows how the attitude error (δ_x, δ_y) is defined near the relaxed hovering condition. Axis $\boldsymbol{x}^b$, $\boldsymbol{y}^b$, and $\boldsymbol{z}^b$ are with respect to body frame.

$$\boldsymbol{R}_b^w \boldsymbol{n}^* = \boldsymbol{e}_3, \tag{7}$$

$$(\boldsymbol{n}^*)^T \sum \boldsymbol{R}_i^b (\boldsymbol{f}_{m,i}^* + \boldsymbol{f}_{a,i}^*) = mg, \tag{8}$$

$$\sum_i (\boldsymbol{\tau}_{m,i} + \boldsymbol{\tau}_{a,i} + \boldsymbol{\tau}_{p,i} + \boldsymbol{\tau}_{r,i}) = \boldsymbol{0} \tag{9}$$

where $(\cdot)^*$ denotes the equilibrium value of $(\cdot)$ in relaxed hovering condition [shown in Fig. 3(a)].

E. Reduced Flight Dynamics

As it is difficult to derive a practical translational controller from such a complex aerodynamic model (5). Here, we use a reduced flight dynamic model to approximate the full translational dynamics based on the relaxed hover condition. With previous analysis, the robot under relaxed hovering conditions can be regarded as a rigid body that rotates at a speed of Ω_n^* around its primary rotating axis $\boldsymbol{n}^*$ and produces a collective thrust T along the rotating axis. Furthermore, we limit our consideration to $\boldsymbol{n}^* \approx [\xi_x^*, \xi_y^*, 1]^T$ with $\xi_x^* \ll 1, \xi_y^* \ll 1$. This means the rotation axis $\boldsymbol{n}^*$ has a small angular deviation from its z axis in the body frame [shown in Fig. 3(a)]. That enables us to approximate the collective thrust T with

$$T = (\boldsymbol{n}^*)^T \sum \boldsymbol{R}_i^b (\boldsymbol{f}_{m,i} + \boldsymbol{f}_{a,i}) \tag{10}$$

$$\approx \sum f_{m,i} \sin\theta_i + \sum f_{l,i} \tag{11}$$

where θ_i is the pitching angle of ith wing module. This implies that the collective force T is related to the sum of motor thrust $(f_{m,i})$ and the lift force $(f_{l,i})$. Again, we take the small deviation assumption $(\xi_x \ll 1, \xi_y \ll 1)$ of $\boldsymbol{n}^*$ and assume the pitching angles are identical for all wings, $\theta_i \approx \theta$. Therefore, it is fair to use the following relation, as $C_{l,i} = C_l, C_{d,i} = C_d$, meaning the lift and drag coefficient for each wing can be regarded as constant values in flight. Combining with (2), we get $f_{l,i} = \frac{C_l}{C_d} f_{d,i}$. With the relaxed hover condition, the torque produced by the tangential component of motor thrust should balance the torque

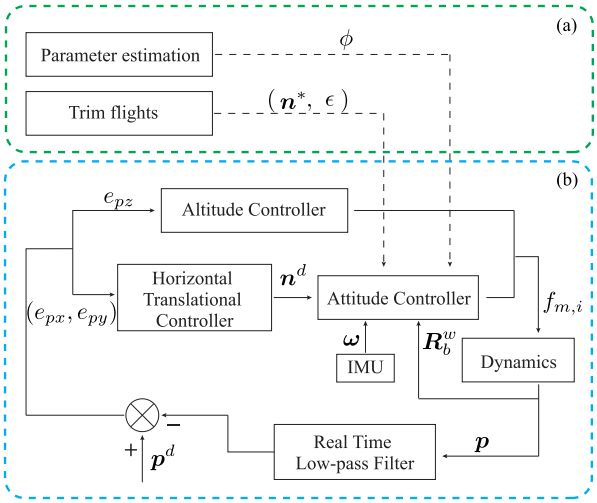

Fig. 4. Proposed flight controller with cascaded structure. (a) illustrates the initialization process for the attitude controller. (b) is the control loop.

caused by drag force, given by

$$\sum f_{m,i} \cos\theta l_m = \sum f_{d,i} l_a = \sum f_{l,i} \frac{C_d}{C_l} l_a \tag{12}$$

where l_a and l_m denote the distance from the rotating axis to the center of pressure and motor respectively. Substituting (12) into (11), we get

$$T \approx c_{f,T} \sum f_{m,i} \tag{13}$$

where $c_{f,T} = \cos\theta \frac{C_l l_m}{C_d l_a} + \sin\theta$, is a constant coefficient describing the relationship of propeller thrust and T. With (13), we obtain reduced translational dynamics from (5), as

$$m\ddot{\boldsymbol{r}} = T\boldsymbol{R}_b^w \boldsymbol{n}^* - mg\boldsymbol{e}_3 \tag{14}$$

which implies that the position can be controlled by maintaining a desired direction of the rotating axis with respect to world frame ($\boldsymbol{R}_b^w \boldsymbol{n}^*$) and the collective thrust T.

IV. Flight Controller Design

In this section, we develop a unified flight control strategy for all different configurations of ARROWs. The controller is designed to be a cascaded structure (shown as Fig. 4). The higher level is a simple proportional controller to minimize the horizontal position error. The lower level is a Lyapunov function candidate-based attitude controller. An altitude controller is created independently by employing a standard proportional-integral-derivative (PID) controller to track the desired height.

A. Attitude Control

1) Attitude Error: In previous section, we introduced a unit vector $\boldsymbol{n}^*$ with respect to the body-fixed frame to represent the attitude of ARROWs under relaxed hover state. Let $\boldsymbol{n}^d$ (a 3×1 unit vector) denote the desired rotation axis in the world frame, then the aim of the attitude controller is to make $\boldsymbol{R}_b^w \boldsymbol{n}^*$ converge to $\boldsymbol{n}^d$, as $\boldsymbol{R}_b^w \boldsymbol{n}^* \to \boldsymbol{n}^d$. Then, the attitude error defined in the body frame can be derived from

$$\boldsymbol{e} = (\boldsymbol{R}_b^w)^T \boldsymbol{n}^d - \boldsymbol{n}^* = \begin{bmatrix} e_x \\ e_y \\ e_z \end{bmatrix} = \begin{bmatrix} \boldsymbol{j}^T \cdot \boldsymbol{n}^d - \xi_x^* \\ \boldsymbol{i}^T \cdot \boldsymbol{n}^d - \xi_y^* \\ 0 \end{bmatrix} \tag{15}$$

where $\boldsymbol{i}$ and $\boldsymbol{j}$ are 3×1 unit vectors to denote the x and y axis of the robot respect to world frame (introduced in Section III-B). We use e_x and e_y to present the angular error in $\boldsymbol{x}^b$ and $\boldsymbol{y}^b$, respectively, (while e_z is not the control objective and considered as zero), even though we notice that the dot product $\boldsymbol{j}^T \cdot \boldsymbol{n}^d$ and $\boldsymbol{i}^T \cdot \boldsymbol{n}^d$ return cosine of the angles. This is because the flight is assumed to be near the hovering state such that the small angle approximation (by employing Taylor series expansion) can be applied, as

$$\begin{aligned} \boldsymbol{j}^T \cdot \boldsymbol{n}^d &= \cos\left(\frac{\pi}{2} + \delta_y\right) \approx -\delta_y, \\ \boldsymbol{i}^T \cdot \boldsymbol{n}^d &= \cos\left(\frac{\pi}{2} + \delta_x\right) \approx -\delta_x \end{aligned} \tag{16}$$

where δ_x and δ_y are small angular deviation of $\boldsymbol{z}^b$ and $\boldsymbol{n}^d$ [shown in Fig. 3(b)].

2) Lyapunov Function Candidate: Let $\boldsymbol{\kappa_p} = \text{diag}(\kappa_{px}, \kappa_{py})$ be a nonnegative gain matrix, we define a vector containing both angular error and angular velocity as $\boldsymbol{s} = \boldsymbol{\kappa}_p [e_x, e_y]^T + [\omega_x, \omega_y]^T$. In addition, we introduce a 2×1 vector $\boldsymbol{\tau}_o = [\tau_{o,x}, \tau_{o,y}]^T$, to denote a constant torque applied on x and y axis in body frame, which is further discussed in Section IV-D. Let $\tilde{\boldsymbol{\tau}}_o$ denote the estimation error, which yields $\boldsymbol{\tau}_o = \hat{\boldsymbol{\tau}}_o + \tilde{\boldsymbol{\tau}}_o$. We propose the Lyapunov function candidate as

$$L = \frac{1}{2}\boldsymbol{s}^T \boldsymbol{s} + \frac{1}{2}\tilde{\boldsymbol{\tau}}_o^T \boldsymbol{\Lambda}^{-1} \tilde{\boldsymbol{\tau}}_o \tag{17}$$

where $\boldsymbol{\Lambda}$ is a 2×2, positive defined adaptive gain matrix. Taking time derivative to L, we obtain

$$\begin{aligned} \dot{L} &= \boldsymbol{s}^T \dot{\boldsymbol{s}} + \dot{\tilde{\boldsymbol{\tau}}}_o^T \boldsymbol{\Lambda}^{-1} \tilde{\boldsymbol{\tau}}_o \\ &= \boldsymbol{s}^T (\boldsymbol{\kappa}_p \boldsymbol{\omega}_{xy} + \dot{\boldsymbol{\omega}}_{xy}) + \dot{\tilde{\boldsymbol{\tau}}}_o^T \boldsymbol{\Lambda}^{-1} \tilde{\boldsymbol{\tau}}_o \end{aligned} \tag{18}$$

where $\boldsymbol{\omega}_{xy} = [\omega_x, \omega_y]^T = [\dot{e}_x, \dot{e}_y]^T$. Considering the attitude dynamics given by (6), $\dot{\boldsymbol{\omega}}_{xy} = [\dot{\omega}_x, \dot{\omega}_y]^T = \boldsymbol{I}_{xy}^{-1}(\boldsymbol{\tau}_{xy} - \boldsymbol{\tau}_o - [\boldsymbol{\omega}_\times \boldsymbol{I}\boldsymbol{\omega}]_{xy})$, where $\boldsymbol{I}_{xy} = \text{diag}(I_{xx}, I_{yy})$, $\boldsymbol{\tau}_{xy} = [\tau_x, \tau_y]^T$, $[\boldsymbol{\omega}_\times \boldsymbol{I}\boldsymbol{\omega}]_{xy}$ is the first two terms of $\boldsymbol{\omega}_\times \boldsymbol{I}\boldsymbol{\omega}$. Submitting $\dot{\boldsymbol{\omega}}_{xy}$ into $\dot{L}$, (18) becomes

$$\begin{aligned} \dot{L} &= \boldsymbol{s}^T (\boldsymbol{\kappa}_p \boldsymbol{\omega}_{xy} + \boldsymbol{I}_{xy}^{-1}(\boldsymbol{\tau}_{xy} - \hat{\boldsymbol{\tau}}_o - \tilde{\boldsymbol{\tau}}_o - [\boldsymbol{\omega}_\times \boldsymbol{I}\boldsymbol{\omega}]_{xy})) \\ &\quad + \dot{\tilde{\boldsymbol{\tau}}}_o^T \boldsymbol{\Lambda}^{-1} \tilde{\boldsymbol{\tau}}_o \\ &= \boldsymbol{s}^T (\boldsymbol{\kappa}_p \boldsymbol{\omega}_{xy} + \boldsymbol{I}_{xy}^{-1}(\boldsymbol{\tau}_{xy} - \hat{\boldsymbol{\tau}}_o - [\boldsymbol{\omega}_\times \boldsymbol{I}\boldsymbol{\omega}]_{xy})) \\ &\quad - \boldsymbol{s}^T \boldsymbol{I}_{xy}^{-1} \tilde{\boldsymbol{\tau}}_o + \dot{\tilde{\boldsymbol{\tau}}}_o^T \boldsymbol{\Lambda}^{-1} \tilde{\boldsymbol{\tau}}_o. \end{aligned} \tag{19}$$

To guarantee $\dot{L} = -\boldsymbol{s}^T \boldsymbol{\kappa}_d \boldsymbol{s} \leq 0$, we derive the control torque from (19), as

$$\boldsymbol{\tau}_{xy} = \hat{\boldsymbol{\tau}}_o + [\boldsymbol{\omega}_\times \boldsymbol{I}\boldsymbol{\omega}]_{xy} - \boldsymbol{I}_{xy} \boldsymbol{\kappa}_p \boldsymbol{\omega}_{xy} - \boldsymbol{I}_{xy} \boldsymbol{\kappa}_d \boldsymbol{s}, \tag{20}$$

where $\boldsymbol{\kappa}_d$ is a nonnegatively defined gain matrix, and $\hat{\boldsymbol{\tau}}_o$ is updated by

$$\dot{\hat{\boldsymbol{\tau}}}_o^T = \boldsymbol{s}^T \boldsymbol{I}_{xy}^{-1} \boldsymbol{\Lambda}. \tag{21}$$

B. Horizontal Translational Control

The horizontal translational controller is designed to eliminate planar position error by controlling the attitude of the robot. Let e_{px} and e_{py} represent the position error in x and y axis, respectively, in world frame. We use magnitude α and direction β to represent the planar error, yielded by

$$\alpha = k_\alpha \sqrt{e_{px}^2 + e_{py}^2}, \quad \beta = \arctan(\frac{e_{py}}{e_{px}}) \tag{22}$$

where k_α is position gain, $\beta \in (-\pi, \pi]$. Considering the condition of near-hovering assumption and the reduced flight dynamics will become difficult to meet when the desired torque goes high, we introduce a parameter to saturate the maximal attitude deviation from the primary rotating axis in the flight, as $|\alpha| \leq \alpha_{\max}$. That is because the differential force of propellers perpendicular to the rotating axis (the residual force projected in the horizontal plane when the spinning speed of propellers is unequal) becomes nonnegligible to generate a high torque. To feed the position error (α, β) into the attitude controller, the desired attitude in (15) is calculated as

$$\boldsymbol{n}^d = \begin{bmatrix} \cos\beta \sin\alpha \\ \sin\beta \sin\alpha \\ \cos\alpha \end{bmatrix}. \tag{23}$$

C. Altitude Control

In this case, the altitude control needs to be considered independently to eliminate the altitude error e_{pz}. With the near-hovering flight condition, we can simplify the considerations by regarding the rotation axis is nearly upright in the flight, which allows us to consider only the collective force T. As a linear-second-order system, a standard PID controller is applied to eliminate the altitude error, which is formulated by

$$T = k_p e_{pz} + k_i \int e_{pz} + k_d \dot{e}_{pz} \tag{24}$$

where k_p, k_i, and k_d are nonnegative gains.

D. Mapping of Control Inputs

In order to implement the attitude controller and translational controller proposed in the previous section, we introduce the mapping of force T, torque $\boldsymbol{\tau}$ and control inputs $f_{m,i}$. The pitching angle and rotary angle of ith of the wing module with respect to the control module are denoted by θ_i and ϕ_i, respectively (shown in Fig. 2).

In the equilibrium state, the aerodynamic forces and torques from the wings are independent of the control signal and balanced with each other, leaving only propeller force f_m, reaction torque τ_r and precession torque τ_p for consideration. Using ϕ and θ, the torque acting on x and y axes can be calculated as

$$\tau_x = \sum((f_{m,i} l_{m,i} s_{\theta_i} + \tau_{r,i} c_{\theta_i}) s_{\phi_i} + \tau_{p,i} c_{\phi_i}), \tag{25}$$

$$\tau_y = \sum(-(f_{m,i} l_{m,i} s_{\theta_i} + \tau_{r,i} c_{\theta_i}) c_{\phi_i} + \tau_{p,i} s_{\phi_i}) \tag{26}$$

where $s_{(\cdot)}$ and $c_{(\cdot)}$ are short for $\sin(\cdot)$ and $\cos(\cdot)$, respectively. Other parameters can be referred to in Fig. 2. Recalling (1), we get the expression of input-related reaction torque, as $\tau_{r,i} = \frac{c_T}{c_f} f_{m,i}$. In the near hovering state, the rotation rate of the robot can be considered as constant value Ω_n^*. Referring to (1) and (4), the magnitude of precession torque can be modeled as

$$\tau_{p,i} = \Omega_n^* I_p \sin\left(\frac{\pi}{2} - \theta_i\right) \Omega_i = \Omega_n^* I_p \cos\theta_i \left(\frac{f_{m,i}}{c_F}\right)^{\frac{1}{2}} \tag{27}$$

where I_p and Ω_i are the moment of inertia along the spinning axis and the spinning speed of ith motor respectively. By employing Taylor series, we can linearize $f_{m,i}^{\frac{1}{2}}$ around its equilibrium point $f_{m,i}^*$, as $f_{m,i}^{\frac{1}{2}} = f_{m,i}|_{f_{m,i}=f_{m,i}^*} + \frac{1}{2} f_{m,i}^{-\frac{1}{2}}|_{f_{m,i}=f_{m,i}^*} (f_{m,i} - f_{m,i}^*) = c_0 + c_1 f_{m,i}$, where $c_0 = f_{m,i}^* - \frac{1}{2}(f_{m,i}^*)^{\frac{1}{2}}$, $c_1 = \frac{1}{2}(f_{m,i}^*)^{-\frac{1}{2}}$ are regarded as constant. Finally, we obtain the linear relationship of $\tau_{p,i}$ and $f_{m,i}$, as

$$\tau_{p,i} = \Omega_n^* I_p \cos\theta_i \left(\frac{c_0}{\sqrt{c_F}} + \frac{c_1}{\sqrt{c_F}} f_{m,i}\right) \tag{28}$$

where the first term is independent to control inputs $f_{m,i}$, which can be balanced by other input-independent torques in the equilibrium state. Taking the same assumption $\theta_i = \theta$ which we introduced in previous Section III-E, and considering that all the wing modules are identical, leading to $l_{m,i} = l_m$, we derive the linear expression of τ_x and τ_y to control inputs $f_{m,i}$, as

$$\tau_x = \sum \left(\left(l_m s_\theta + \frac{c_T}{c_F} c_\theta \right) s_{\phi_i} + \frac{\Omega_n^* I_p c_\theta c_1}{\sqrt{c_F}} c_{\phi_i} \right) f_{m,i}, \tag{29}$$

$$\tau_y = \sum \left(- \left(l_m s_\theta + \frac{c_T}{c_F} c_\theta \right) c_{\phi_i} + \frac{\Omega_n^* I_p c_\theta c_1}{\sqrt{c_F}} s_{\phi_i} \right) f_{m,i}. \tag{30}$$

However, in practice, it is difficult to obtain all the precise parameters to calculate τ_x and τ_y. In order to minimize the impact due to parameter uncertainty, we define $\lambda \sin\epsilon := l_m \sin\theta + \frac{c_T}{c_F} \cos\theta$, $\lambda \cos\epsilon := \frac{\Omega_n^* I_p \cos\theta c_1}{\sqrt{c_F}}$. Substituting them into (29) and (30), we obtain a simplified expression, $\tau_x = \sum(\sin\epsilon \sin\phi_i + \cos\epsilon \cos\phi_i)\lambda f_{m,i}$, $\tau_y = \sum(-\sin\epsilon \cos\phi_i + \cos\epsilon \sin\phi_i)\lambda f_{m,i}$. In this way, λ becomes a scalar of motor thrust, which can be handled by adjusting the proportional gain of the controller. ϵ is a constant denoting the ratio of the collective torque caused by τ_r, f_m and the torque caused by precession motion τ_p (shown in Fig. 2), and is determined experimentally. Combining (13), we obtain the linear mapping to control input $\boldsymbol{u}$, as

$$\begin{bmatrix} \tau_x \\ \tau_y \\ T \end{bmatrix} = \overbrace{\begin{bmatrix} s_\epsilon s_{\phi_1} + c_\epsilon c_{\phi_1}, s_\epsilon s_{\phi_i} + c_\epsilon c_{\phi_i}, .. \\ -s_\epsilon c_{\phi_1} + c_\epsilon s_{\phi_1}, -s_\epsilon c_{\phi_i} + c_\epsilon s_{\phi_i}, .. \\ 1, 1, .. \end{bmatrix}}^{\boldsymbol{A}^{3\times n}} \overbrace{\begin{bmatrix} f_1 \\ f_i \\ .. \end{bmatrix}}^{\boldsymbol{u}^{n\times 1}} \tag{31}$$

where $\boldsymbol{A}$ is the configuration matrix, $\boldsymbol{u}$ is the motor input vector.

E. Implementation Considerations

To implement the proposed flight controller in different configurations, we discuss the situation in the following aspects:

1) Attitude Controller Modification: The attitude controller designed in Section IV-A considers two parts: 1) the attitude error; and 2) the constant torque due to the asymmetric configuration [refer to (17)]. However, in practice, only the configurations with vertical installed rotors ($\theta = 90^\circ$) need to use the adaptive term to actively compensate the unbalanced torque $\boldsymbol{\tau}_o$. For the configurations with self-rotation motion ($\theta \ll 90^\circ$), the unbalanced torque $\boldsymbol{\tau}_o$ is cancelled in its relaxed hovering condition. Thus, in those cases, the adaptive gain $\boldsymbol{\Lambda}$ is set to zero.

In addition, the control torque (20) derived from the proposed Lyapunov function (17) consists of both angular error and the angular velocity. In practical implementation, it is difficult to make use of the angular velocity to stabilize the flight attitude. That's because the high self-rotating speed (around 30–60 rd/s) has significant components on $\boldsymbol{x}^b$ and $\boldsymbol{y}^b$ axis when $\boldsymbol{z}^b$ is not aligned with the rotating axis $\boldsymbol{n}$. Even the small angle deviation assumption has been made to ξ_x and ξ_y; the components of the rotating speed Ω_n on each primary axis of body frame are still nonnegligible and have critical impact on attitude control. As a result, we consider only the attitude error practically, and (17) becomes

$$\boldsymbol{\tau}_{xy} = -\boldsymbol{I}_{xy}\boldsymbol{\kappa}_p[e_x, e_y]^T. \tag{32}$$

On the other hand, the high self-rotating speed also allows the robot to benefit from the gyroscopic effect, which offers the passive damping ability to the attitude stabilization [40].

2) Implementation on the Case When $N < 3$: For the configurations when wing number $n < 3$, the system is not able to generate enough independent control signals to all the τ_x, τ_y, and T due to the severe underactuation. Thanks to the fast rotation motion, the control signal for attitude stabilization is nearly cyclic, which limits the impact of the motor speed on altitude dynamics over a cycle. This also motivates us to control the position and attitude with different controller in parallel, as

$$C_m = C_h + C_a \tag{33}$$

where C_h is the command generated by altitude controller [shown in (24)], C_a is the command generated by attitude controller [shown in (20)]. And $\boldsymbol{A}$ becomes a 2×2 matrix.

3) Implementation on the Case When $N \geq 3$: When the number of wing module $n \geq 3$, the proposed system is able to produce at least 3 independent controlling signals. In this case, τ_x, τ_y, and T are calculated by attitude and altitude controller, respectively. And the actuator input $\boldsymbol{u}$ can be directly calculated by inverting ($n = 3$) or pseudoinverting ($n > 3$) matrix $\boldsymbol{A}$.

4) Implementation on the Case When the Rotors are Vertically Installed: When the wing modules are perpendicularly installed to the control module, the input mapping can be directly obtained from (29) and (30) by substituting $\theta = \frac{\pi}{2}$ (in radians).

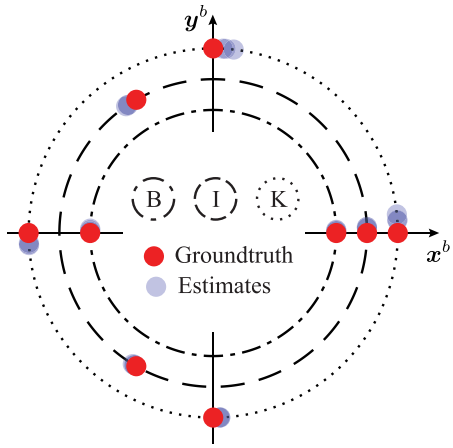

Fig. 5. ϕ estimation for configuration B, I, and K. Red color is the groundtruth, blue color represents estimations.

F. Parameter Estimation

Owing to the reconfiguration, the relative attitude (ϕ, θ) of the control module and wing module may change, leaving some dynamic uncertainties to the robot. With previous analysis, the uncertainties caused by θ is covered by introducing parameter ϵ. To obtain matrix $\boldsymbol{A}$, here, we leverage multiple IMUs for estimating angle ϕ. Let $\boldsymbol{\omega}^b$ represent the angular velocity in robot's body frame (control module) and $\boldsymbol{\omega}^i$ represent the angular velocity of the ith wing module. Considering each module experiences the same angular velocity with respect to body frame, we then have the relations as shown by

$$\boldsymbol{\omega}^b = \boldsymbol{R}_i^b \boldsymbol{\omega}^i. \tag{34}$$

By employing multiple variable regression, we can calculate the rotation matrix $\boldsymbol{R}_i^b$. It is fair to assume that the y axis of the wing module is pointing to the center of the control module and parallel to the plane formed by x–y axes. Then, the angle ϕ_i can be derived by calculating the angle between x axis of control module and y axis of the wing module with respect to the body frame, as

$$\cos\phi_i = \boldsymbol{e}_1 \cdot (-\boldsymbol{R}_i^b(:, 2)) \tag{35}$$

where $\boldsymbol{e}_1 = [1, 0, 0]^T$, $\boldsymbol{R}_i^b(:, 2)$ is the second column of $\boldsymbol{R}_i^b$, which represents the y axis of ith wing module in control module frame.

V. Experimental Validation

A. Preflight Estimation

In order to obtain a suitable range of gyroscopic readings for all the IMUs, the prototype was handheld and manually rotated in each trial, similarly in [3]. All the IMU data were collected and saved by running a Python (Pycharm) script with multiple threads on the ground-station via WIFI. The data collection period was 20 s with a sampling frequency at around 100 Hz. Since the data of each modules were saved with different time stamp, we first need to create a common timeline by combining

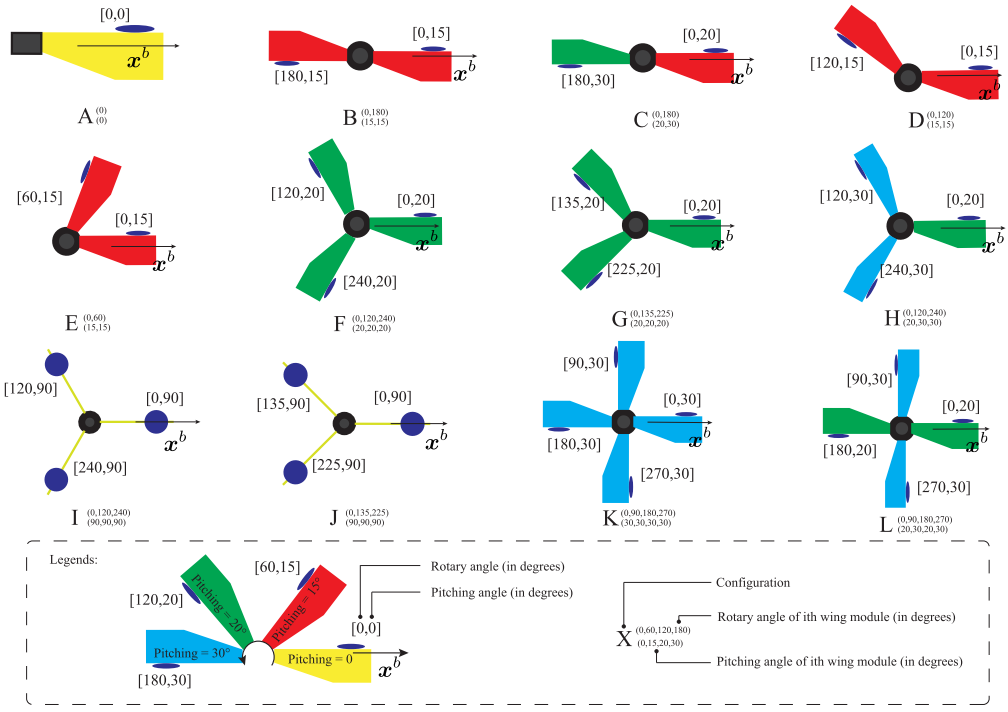

Fig. 6. Details of a total of 12 different configurations which are tested in flight experiments. The number of wing modules n varies from 1 to 4. Different rotary angle ϕ and pitching angle θ are combined.

all the saved time stamp together. Let t_i represent the time stamp of the ith IMU module, then the common time line is defined as $t_c = [t_1, t_2, t_i, ..]$. Next, each recorded IMU reading needed to be interpolated to align with the common time line, t_c. Let the gyroscopic reading of ith IMU be g_i, then the interpolation is processed as, $g_i' = interp(t_i, g_i, t_c)$, where $interp$ is a interpolation function. With g_i' and t_c, we can calculate the relative rotary angle by processing via (34) and (35).

The estimation results as plotted in Fig. 5 validated the proposed estimating method. The average absolute errors for configuration (b), (i), and (k) is 1.3°, 2.4°, 3.4°, respectively. The possible factors could come from the data processing, such as the linear regression and interpolation, and the IMU installation error.

B. Flight Experiment

To quantify the flight performance, we carried out several types of flight experiments including hovering, helical-trajectory tracking, and step trajectory tracking. In total, there were 12 different platforms tested with various of combinations of the number of wing module, pitching angles, and rotary angles, details shown in Fig. 6.

1) Experimental Setup: All flight experiments were conducted in an indoor environment equipped with motion capture cameras. The communication between onboard flight controller (Crazyflie Bolt) and ground-station is through radio communication (Crazyradio PA). Other details can be found by our previous publication [34].

TABLE I
ROTATING AXIS IN RELAXED HOVERING STATE

Configuration	A	C	D	E
$[\xi_x^*, \xi_y^*]$ in degrees	[4.6, 28]	[0.3, 3.8]	[-1.3, 3.2]	[-3.4, 10.1]
Configuration	G	H	I, J	Others
$[\xi_x^*, \xi_y^*]$ in degrees	[2, -3]	[0.74, -1]	NP	[0, 0]

2) Trim Flights: With preflight estimation introduced in Section V-A, ϕ angles for each configuration were obtained. Trim flights needed to be carried out to determine the value of ξ_x^* and ξ_y^* in (15) and parameter ϵ in matrix $\boldsymbol{A}$. Details of ξ_x^* and ξ_y^* are listed in Table I. ϵ was roughly decided experimentally. We found that the attitude can be stabilized when choose $\epsilon = \frac{\pi}{3} \pm \frac{\pi}{10}$ (in radians) for all the configurations except (i) and (j).

3) Hovering Flights: We conducted a 90-s hovering flight for all the configurations given in Fig. 6, including takeoff, hovering, and landing. With experimentally determined parameters, we tested the hovering flight with a desired position at $[0, 0, 1.2]$ in order to be free of ground effect. The flight performance of both position and attitude control was evaluated by the average and standard deviation of absolute position and attitude error. Since takeoff and landing was initialized manually by a transmitter, the time interval selected for evaluation was taken from 20–80 s. And each flight was repeated for five times. Details of position and attitude plot can be found in Fig. 7.

Compared to other configurations, Fig. 7(i) and (j) have much simpler force model thanks to the vertical installed wing modules and slow rotating speed (around 0.1 m/s, gyroscopic effect can be ignored). As a result, Fig. 7(i) and (j) have better capability

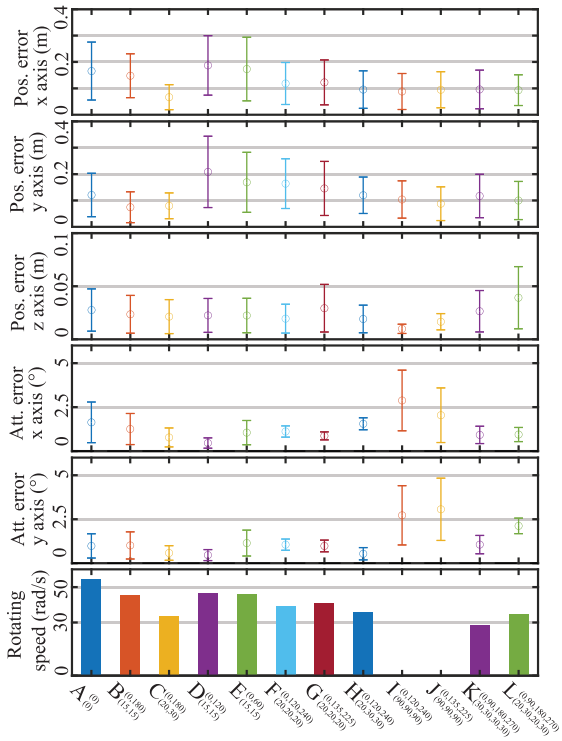

Fig. 7. Average and standard deviation of absolute position and attitude error in hovering flights. The plots are calculated from five flights with the time intervals of 20–80 s.

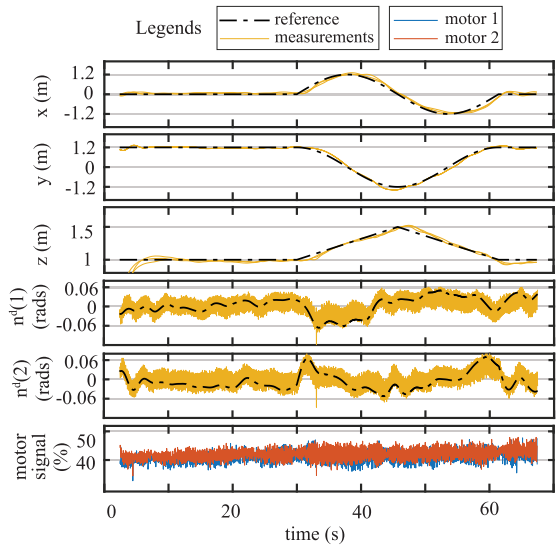

Fig. 8. Trajectories and attitude plots of helical tracking for Section V-B-4. First three subplots show the trajectories with three flights in *x*, *y*, and *z* axis, respectively. Next two subplots show the desired flight attitude (rotation axis $\boldsymbol{n}^d$) calculated by planar translational controller (black dashed line) versus *z* axis of robot with respect to the inertia frame. The last plot shows the normalized motor signals.

(in contrast to other rotating configurations) to respond to the position error. However, the unbalanced reaction torques from propellers (all are in the same spinning direction) cause the uncertain and varying yaw value in the hovering flight, which results in unexpected attitude errors [see (15)]. Consequently, the flight performance of Fig. 7(i) and (j) shows high attitude

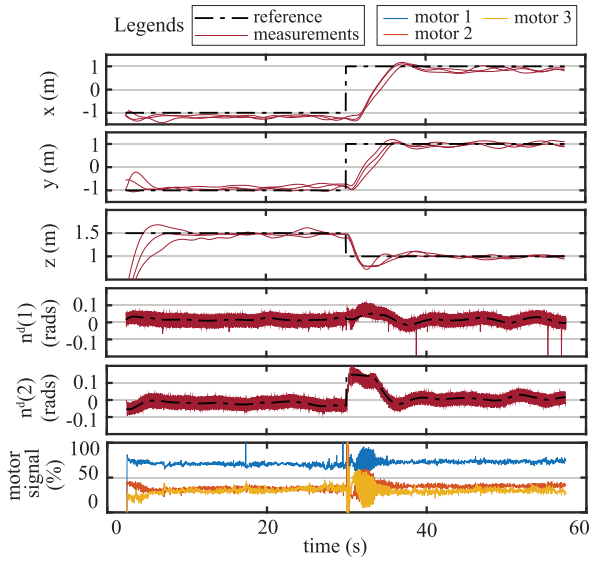

Fig. 9. Trajectories and attitude plots of step tracking for Section V-B-5. First three subplots show the trajectories with three flights in *x*, *y*, and *z* axis, respectively. Next two subplots show the desired flight attitude (rotation axis $\boldsymbol{n}^d$) calculated by planar translational controller (black dashed line) versus *z* axis of robot with respect to the inertia frame. The last plot shows the normalized motor signals.

error but relatively small position error compared to other configurations.

Unlike Fig. 7(i) and (j), the rest of platforms have much smaller pitching angle and higher rotating speed. Note that the higher rotating speed introduces higher angular momentum [40], which requires higher torque generation for attitude stabilization, accordingly. What's more, the lower pitching angles will decrease the torque generation ability based on (29) and (30). As a result, platform (c) in Fig. 7 has more difficulties when stabilizing the flight attitude (explained in Section IV-B), and that's why platform (c) shows both higher attitude and position error than (b) even with asymmetric configuration in Fig. 7.

To avoid the large torque generation and maintain the reduced flight dynamics assumption, the angular deviation saturation value $\alpha_{\max}$ and position gain k_α are set relative smaller in some configurations such as (d) and (e), to achieve a stable flight. As a result, the position holding performance becomes worse while the attitude error maintains small.

When the number of wing modules $n \geq 3$, the ARROWs is able to stabilize its flight attitude without relying on passive stability. However, extra wing modules also increase the total mass, the moment of inertia, and rotating speed, which requires high torque generation to overcome the damping effect caused by the high angular momentum [40]. Combined with our previous analysis in Section IV-B, that explains why the flight performance does not show better by simply increasing the number of wing modules when comparing platforms (f), (g), (h), (k), (l) to (a), (b), (c). It seems that the configuration with two symmetrically installed wing modules shows better flight performance among all as it has a relatively large torque generation capacity (compared to $n = 1$) and small moment of inertia (compared to $n = 3, 4$).

TABLE II
FLIGHT DURATION TEST

Configuration	A	B	F	K	I
Weight (g)	63	107	134	138	161
Flight time (s)	523	399	281	259	216

In order to show the power efficiency with different numbers of wing modules, we also carried out the flight duration test (with a 300-mAh Li-Po battery for all flights) for configurations (a), (b), (f), (i), (k). Each flight has been repeated three times. Average flight duration is given in Table II. During the test, the robots are controlled at the same reference position [0, 0, 1.2]. Compared to configuration (i), which generates the lifting force directly by the propeller, (f) shows around 30% longer flight time without particular optimization.

4) Helical Trajectory Tracking: A helix-like trajectory (with radius of 1.2 m) was chosen for configurations (a), (b), (c), (d), and (e), to evaluate the flight performance in slow speeds (with average horizontal translational speed at 0.25 m/s). In the first 30 s, the robot took off from ground and hovered at 1-m height. From 30 to 60 s, robot tracked the helical trajectory with constantly moving height setpoints from 1 to 1.5 m.

We have chosen configuration (c) to show the flight details of helical trajectory tracking as it has unequal pitching angles. The flight was repeated three times, and one of them is chosen to show the attitude control performance and the corresponding normalized motor command signal as shown in Fig. 8.

5) Step Trajectory Tracking: A step trajectory with different altitude setpoints was developed for configurations (f), (g), (h), (i), (j), (k), and (l). For the first 30 s, the robot was manually triggered to takeoff and hovered at $[-1, -1, 1.5]$. For 30 s to 60 s, the setpoint was shifted to $[1, 1, 1]$. Each flight was repeated three times. We select configuration (g) to show the details of flight in Fig. 9 as it has unequal rotary angles ϕ. The average speed of translational motion was around 0.3 m/s.

VI. CONCLUSION

In this work, we have developed a modular aerial robotic platform: ARROWs. With simple human assistance, ARROWs can be reconstructed into different configurations with various wing numbers, and rotary and pitching angles. With some necessary assumptions, we modeled and studied the reduced flight dynamics of the proposed robots. The insights motivate us to design a practical flight controller with a cascaded structure. To overcome the possible dynamical uncertainties caused by the nature of reconfiguration, we also introduced an IMU-based rotary angle estimation strategy. To evaluate the proposed platforms and flight controller, 12 configurations with different wing numbers and pitching angles were tested in actual flights. All configurations showed stable flight performance and the potential of the applications.

The findings of the experiments validate the advantage of the proposed modular aerial robotic platform in the following aspects. First, the ability of reconfiguration enables ARROWs to work with selected features, such as the footprint, flight duration, and payload capacity. In addition, the huge airfoils allow ARROWs to become more power efficient than those traditional multirotors generating thrust directly with propellers. Lastly, the inherited passive rotating motion can provide convenience to some of the potential applications. For example, the Li-DAR and camera would obtain a wider view with a proper rotating speed. As the flight controller is developed based on the near-hovering state to simplify the complexity caused by the aerodynamics and rotary motion, the main limitation of ARROWs is its insufficiency of agility. On the other hand, the existence of inherited self-rotating motion can also become a problem when the payload is sensitive to rotation. Another limitation of this research is the proposed cascaded flight controller necessities the decoupling of the attitude dynamics and translational dynamics. However, this condition is difficult to satisfy in some configurations. Details are explained in Section IV-B.

To break those limitations of this research as discussed above, future works can be expected as follows. First, an optimized flight configuration including wing numbers, wing geometry, and pitching angle can be studied to balance the payload capacity, hovering efficiency as well as control authority. Besides, a robotic platform with multiple flight modes can be explored to address the problem caused by the insufficient agility of ARROWs.

REFERENCES

[1] R. Mahony, V. Kumar, and P. Corke, "Multirotor aerial vehicles: Modeling, estimation, and control of quadrotor," *IEEE Robot. Automat. Mag.*, vol. 19, no. 3, pp. 20–32, Sep. 2012.

[2] D. Floreano and R. J. Wood, "Science, technology and the future of small autonomous drones," *Nature*, vol. 521, no. 7553, pp. 460–466, 2015.

[3] B. Mu and P. Chirarattananon, "Universal flying objects: Modular multirotor system for flight of rigid objects," *IEEE Trans. Robot.*, vol. 36, no. 2, pp. 458–471, Apr. 2020.

[4] D. Saldana, B. Gabrich, G. Li, M. Yim, and V. Kumar, "Modquad: The flying modular structure that self-assembles in midair," in *Proc. IEEE Int. Conf. Robot. Automat.*, 2018, pp. 691–698.

[5] R. Oung and R. D'Andre,, "The distributed flight array: Design, implementation, and analysis of a modular vertical take-off and landing vehicle," *Int. J. Robot. Res.*, vol. 33, no. 3, pp. 375–400, 2014.

[6] S. Bai and P. Chirarattananon, "Splitflyer air: A modular quadcopter that disassembles into two bicopters mid-air," *IEEE/ASME Trans. Mechatronics*, vol. 27, no. 6, pp. 4729–4740, Dec. 2022.

[7] H. Jia et al., "A quadrotor with a passively reconfigurable airframe for hybrid terrestrial locomotion," *IEEE/ASME Trans. Mechatronics*, vol. 27, no. 6, pp. 4741–4751, Dec. 2022.

[8] Y. H. Tan and B. M. Chen, "Thruster allocation and mapping of aerial and aquatic modes for a morphable multimodal quadrotor," *IEEE/ASME Trans. Mechatronics*, vol. 25, no. 4, pp. 2065–2074, Aug. 2020.

[9] X. Tao, N. Lang, H. Li, and D. Xu, "Path planning in uncertain environment with moving obstacles using warm start cross entropy," *IEEE/ASME Trans. Mechatronics*, vol. 27, no. 2, pp. 800–810, Apr. 2022.

[10] Y. Zhu, Z. Wang, C. Chen, and D. Dong, "Rule-based reinforcement learning for efficient robot navigation with space reduction," *IEEE/ASME Trans. Mechatronics*, vol. 27, no. 2, pp. 846–857, Apr. 2022.

[11] Z. Wang, Z. Qian, Z. Song, H. Liu, W. Zhang, and Z. Bi, "Instrumentation and self-repairing control for resilient multi-rotor aircrafts," *Ind. Robot: An Int. J.*, vol. 45, no. 5, pp. 647–656, 2018.

[12] M. Zhao, T. Anzai, F. Shi, X. Chen, K. Okada, and M. Inaba, "Design, modeling, and control of an aerial robot dragon: A dual-rotor-embedded multilink robot with the ability of multi-degree-of-freedom aerial transformation," *IEEE Robot. Automat. Lett.*, vol. 3, no. 2, pp. 1176–1183, Apr. 2018.

[13] D. Falanga, K. Kleber, S. Mintchev, D. Floreano, and D. Scaramuzza, "The foldable drone: A morphing quadrotor that can squeeze and fly," *IEEE Robot. Automat. Lett.*, vol. 4, no. 2, pp. 209–216, Apr. 2019.
[14] Ö. G. Y. Eraslan, Ö. Enes, and T. Oktay, "The effect of change in angle between rotor arms on trajectory tracking quality of a pid controlled quadcopter."
[15] H. Şahin, O. Kose, and T. Oktay, "Simultaneous autonomous system and powerplant design for morphing quadrotors," *Aircr. Eng. Aerosp. Technol.*, vol. 94, no. 8, pp. 1228–1241, 2022.
[16] O. Kose and T. Oktay, "Simultaneous quadrotor autopilot system and collective morphing system design," *Aircr. Eng. Aerosp. Technol.*, vol. 92, no. 7, pp. 1093–1100, 2020.
[17] H. Bhardwaj, X. Cai, S. K. H. Win, and S. Foong, "Design, modeling and control of a two flight mode capable single wing rotorcraft with mid-air transition ability," *IEEE Robot. Automat. Lett.*, vol. 7, no. 4, pp. 11720–11727, Oct. 2022.
[18] K. Mohammadi, S. Sirouspour, and A. Grivani, "Control of multiple quad-copters with a cable-suspended payload subject to disturbances," *IEEE/ASME Trans. Mechatronics*, vol. 25, no. 4, pp. 1709–1718, Aug. 2020.
[19] J. Daudelin, G. Jing, T. Tosun, M. Yim, H. Kress-Gazit, and M. Campbell, "An integrated system for perception-driven autonomy with modular robots," *Sci. Robot.*, vol. 3, no. 23, 2018, Art. no. eaat 4983.
[20] J. Paulos et al., "Automated self-assembly of large maritime structures by a team of robotic boats," *IEEE Trans. Automat. Sci. Eng.*, vol. 12, no. 3, pp. 958–968, Jul. 2015.
[21] F. Wang, Z. Qian, Z. Yan, C. Yuan, and W. Zhang, "A novel resilient robot: Kinematic analysis and experimentation," *IEEE Access*, vol. 8, pp. 2885–2892, 2019.
[22] J. Wu, C. Yuan, R. Yin, W. Sun, and W. Zhang, "A novel self-docking and undocking approach for self-changeable robots," in *Proc. IEEE 4th Inf. Technol., Networking, Electron. Automat. Control Conf.*, 2020, vol. 1, pp. 689–693.
[23] T. Zhang, W. Zhang, and M. M. Gupta, "Resilient robots: Concept, review, and future directions," *Robotics*, vol. 6, no. 4, p. 22, 2017.
[24] D. Saldana, P. M. Gupta, and V. Kumar, "Design and control of aerial modules for inflight self-disassembly," *IEEE Robot. Automat. Lett.*, vol. 4, no. 4, pp. 3410–3417, Oct. 2019.
[25] M. W. Mueller and R. D'Andrea,, "Relaxed hover solutions for multicopters: Application to algorithmic redundancy and novel vehicles," *Int. J. Robot. Res.*, vol. 35, no. 8, pp. 873–889, 2016.
[26] W. Zhang, M. W. Mueller, and R. D'Andrea, "A controllable flying vehicle with a single moving part," in *Proc. IEEE Int. Conf. Robot. Automat.*, 2016, pp. 3275–3281.
[27] M. Piccoli and M. Yim, "Passive stability of a single actuator micro aerial vehicle," in *Proc. IEEE Int. Conf. Robot. Automat.*, 2014, pp. 5510–5515.
[28] J. Paulos and M. Yim, "Flight performance of a swashplateless micro air vehicle," in *Proc. IEEE Int. Conf. Robot. Automat.*, 2015, pp. 5284–5289.
[29] E. R. Ulrich, D. J. Pines, and J. S. Humbert, "From falling to flying: The path to powered flight of a robotic samara nano air vehicle," *Bioinspiration Biomimetics*, vol. 5, no. 4, 2010, Art. no. 045009.
[30] S. K. H. Win, L. S. T. Win, D. Sufiyan, and S. Foong, "Design and control of the first foldable single-actuator rotary wing micro aerial vehicle," *Bioinspiration Biomimetics*, vol. 16, no. 6, 2021, Art. no. 066019.
[31] S. Bai, Q. He, and P. Chirarattananon, "A bioinspired revolving-wing drone with passive attitude stability and efficient hovering flight," *Sci. Robot.*, vol. 7, no. 66, 2022, Art. no. eabg 5913.
[32] R. Å. Norberg, "Autorotation, self-stability, and structure of single-winged fruits and seeds (samaras) with comparative remarks on animal flight," *Biol. Rev.*, vol. 48, no. 4, pp. 561–596, 1973.
[33] S. K. H. Win, L. S. T. Win, D. Sufiyan, G. S. Soh, and S. Foong, "An agile samara-inspired single-actuator aerial robot capable of autorotation and diving," *IEEE Trans. Robot.*, vol. 38, no. 2, pp. 1033–1046, Apr. 2022.
[34] X. Cai, S. K. H. Win, L. S. T. Win, D. Sufiyan, and S. Foong, "Cooperative modular single actuator monocopters capable of controlled passive separation," in *Proc. Int. Conf. Robot. Automat.*, 2022, pp. 1989–1995.
[35] K. Y. Ma, P. Chirarattananon, S. B. Fuller, and R. J. Wood, "Controlled flight of a biologically inspired, insect-scale robot," *Science*, vol. 340, no. 6132, pp. 603–607, 2013.
[36] C. H. Tan, D. S. bin Shaiful, E. Tang, G. S. Soh, and S. Foong, "Flydar: A passive scanning flying lidar sensing system for slam using a single laser," *IEEE Sensors J.*, vol. 22, no. 2, pp. 1746–1755, Jan. 2022.
[37] M. Bangura, M. Melega, R. Naldi, and R. Mahony, "Aerodynamics of rotor blades for quadrotors," 2016, *arXiv:1601.00733*.
[38] Y. Lee, K.-B. Lua, T. Lim, and K. Yeo, "A quasi-steady aerodynamic model for flapping flight with improved adaptability," *Bioinspiration Biomimetics*, vol. 11, no. 3, 2016, Art. no. 036005.
[39] H. Semat and R. Katz, "Physics, chapter 11: Rotational motion (the dynamics of a rigid body)," *Robert Katz Pub.*, p. 141, 1958.
[40] S. H. Crandall, "The effect of damping on the stability of gyroscopic pendulums," in *Theoretical, Experimental, and Numerical Contributions to the Mechanics of Fluids and Solids*. Berlin, Germany: Springer, 1995, pp. 761–780.

Xinyu Cai received the B.S. degree in mechanical engineering from Donghua University, Shanghai, China, in 2015, and the M.Phil. degree in biomedical engineering from the City University of Hong Kong, Hong Kong, in 2020. He is currently working toward the Ph.D. degree with the pillar of Engineering Product Development (EPD), Singapore University of Technology and Design, Singapore.

His research interests include the development, control, and application of aerial robotic systems.

Shane Kyi Hla Win received the B.E. and Ph.D. degrees in mechanical engineering from the Singapore University of Technology and Design (SUTD), Singapore, in 2015 and 2020, respectively.

He is currently a Postdoctoral Research Fellow with Temasek Laboratories, SUTD. His current research involves optimizing the design and modeling Samara autorotating wings (SAW) for lightweight payload delivery and single actuator monocopter (SAM). His research interests include nature-inspired UAVs, optimization of design parameters, flight dynamics, and flight control of UAVs.

Hitesh Bhardwaj received the B.Eng. degree in aerospace engineering from the University of the West of England, Bristol, U.K., in 2014, and the M.Sc. degree in aeronautical engineering from Politecnico di Milano, Milan, Italy, in 2017. He is currently working toward the Ph.D. degree with the pillar of Engineering Product Development (EPD), Singapore University of Technology and Design (SUTD), Singapore. His Ph.D. is focused on the implementation of multiple actuators on the nature-inspired monocopter platform.

His research interests include robotics, system modeling and control through simulation, flight dynamics, and nature-inspired UAVs.

Shaohui Foong (Member, IEEE) received the B.S., M.S., and Ph.D. degrees in mechanical engineering from the George W. Woodruff School of Mechanical Engineering, Georgia Institute of Technology, Atlanta, GA, USA, in 2005, 2008, and 2010, respectively.

In 2011, he was a Visiting Assistant Professor with the Massachusetts Institute of Technology, Cambridge, MA, USA. He is an Associate Professor with the Engineering Product Development (EPD) Pillar, Singapore University of Technology and Design (SUTD), Singapore, and a Visiting Academician with Changi General Hospital, Singapore. His research interests include system dynamics and control, nature-inspired robotics, magnetic localization, medical devices, and design education and pedagogy.